Journal of Ovonic Research Vol. 20, No. 3, May - June 2024, p. 405 - 415

Tungsten oxide nanomaterial interactions below monolayer coverage

F. Aguilera[a], M. Cota- Leal[b], P. Luque[c], A. Olivas[b*]
[a]*Autonomous University of Baja California, Faculty of Engineering, Architecture and Design – Doctorate Program in Sciences and Engineering, CP 22860, Ensenada, B.C., Mexico*
[b]*National Autonomous University of Mexico, Center for Nanosciences and Nanotechnology, CP 22860, Ensenada, B.C., Mexico*
[c]*Autonomous University of Baja California, Faculty of Engineering, Architecture and Design, CP 22860, Ensenada, B.C., Mexico*

A tungsten oxide load at submonolayer coverage of alumina renders highly dispersed dimeric polytungstate (octahedral and distorted octahedral coordination) and isolated monotungstate (tetrahedral) species. The polytungstate/monotungstate proportion increases when approaching monolayer. Crystalline WO_3 nanoparticles emerge at higher loads. All components display hexavalent oxidation; yet, tungsten- oxide (W–O–W) and tungsten- oxide- alumina (W–O–Al) interactions were discerned by X- ray photoelectron spectroscopy of the WO_x/Al_2O_3 materials herein prepared with 1, 3, and 5 weight percentages. The 5 *wt* % sample displayed the highest intensity percentage of W–O–Al species correlated to the highest methanol conversion (45 %), ascribed to the appearance of the weak acidity disclosed by temperature- programmed desorption of ammonia.

(Received October 27, 2023; Accepted June 14, 2024)

Keywords: Tungsten, Metal surface density, Nanomaterials, Low metal load, XPS

1. Introduction

Nanomaterials based on the transition- metal tungsten (W) play a pivotal role in advancing various technological applications for their characteristics reflected in a high melting temperature and intrinsic photo electrochromic, toughness, and mechanical properties. They are regarded as potential candidates for optical and electrical uses [1 – 5] and are widely sought after for their adjustable catalyst character in chemical reactions of large- scale production; moreover, they provide the stackable benefit of low cost and availability [6, 7].

The fine- tuning of supported tungsten oxide (WO_x) catalysts renders them highly selective for several reactions including hydrothermal [8], metathesis [9 – 11], photocatalytic [4 – 5, 12 – 14], petrochemical cracking [15], and other environment- related reactions [16 – 17].

The aforementioned array of materials highlights the importance of the intricate relation between performance and characteristics such as selected support, overall particle composition, specific surface area, particle size, distribution of active phase, and metal oxide- support interaction. This relation can be streamlined by tailoring the synthesis processes by varying methodologies, specific precursor salts, metal loading, calcination temperature, and reduction pre- treatment, to name a few.

A deep understanding of the tungsten oxide supported on alumina system (WO_3/Al_2O_3) has been a long- standing process carried out through various research groups and characterization techniques such as Raman, X- ray Diffraction, Ion Scattering, X- ray Absorption Near- Edge, UV- vis Diffuse Reflectance, High- Resolution Transmission Electron, and X- ray Photoelectron Spectroscopies [18 – 20]. It is currently accepted that tungsten oxide can exist with different molecular and electronic structures depending on metal loading rather than on the oxide support (Al_2O_3, TiO_2, Nb_2O_5, ZrO_2, SiO_2) [21, 22]. Monolayer coverage of moderately aggregate polytungstate has been theoretically established to occur near 5 W nm^{-2} surface density considering the 0.22 nm^{-2} cross- section area of an octahedrally coordinated or distorted octahedral (unsaturated) WO_x molecule. At submonolayer, < 5 W nm^{2}, highly dispersed dimeric

* Corresponding author: aolivas@ens.cnyn.unam.mx
https://doi.org/10.15251/JOR.2024.203.405

polytungstate and isolated monotungstate are present with tetrahedral coordination. Whereas, above 5 tungsten surface density coverage, > 5 W nm^{-2}, large aggregates of crystalline WO_3 nanoparticles sit on top of the monolayer and sometimes portray bulk- like properties [9, 15, 23 – 26].

Since WO_3 nanoparticles above the monolayer have lower interaction with the support, they can be reduced leading to oxygen vacancies due to the multivalence character of tungsten down to the metallic state [26]. Crystalline WO_3 tends to be inert in acidic- dependent chemical reactions [27]. On the other hand, the strong support- interacting tungsten species at or below monolayer are non- reducible and can affect the Lewis and/or Brønsted acidic properties of the WO_3/Al_2O_3 catalysts [21, 23, 26 – 30].

As noted above, X- ray photoelectron spectroscopy (XPS) is a powerful tool for assessing the chemical environment of material surface and metal- support interphase. The oxidation states disclosed about the components provide additional leverage for gaining a more thorough comprehension of the active sites of the catalysts.

In this study, nanoparticles (NPs) of tungsten oxide supported on a mixed- phase alumina were prepared with a metal load below and close to monolayer through the dry impregnation method. All the samples were characterized by physicochemical techniques such as Thermogravimetric analysis (TGA) and differential scanning calorimetry (DSC), X- ray Diffraction (XRD), High- Resolution Transmission Electron Microscopy (HRTEM) and Select Area Electron Diffraction (SAED), Scanning Electron Microscopy (SEM) and energy- dispersive X- ray spectrometry (EDS), N_2 Adsorption- desorption, X- ray Photoelectron Spectroscopy (XPS), Temperature Programmed Desorption of Ammonia (TPD- NH_3). We identified two tungsten species (W–O–W and W–O–Al) on the surface of the NPs. Both species were correlated to the surface reactivity properties of the NPs evaluated through steady- state dehydration of methanol to dimethyl ether (DME).

2. Experimental

2.1. Materials preparation

All reagents were used as received, and no previous purification was performed. The nanomaterials were prepared via the impregnation method, with different amounts of ammonium tetrathiotungstate ($(NH_4)_2WS_4$, ATT) (Aldrich, 99.9 %) over commercial alumina, Al_2O_3, (Alfa Aesar, super activated, acidic, 50 – 200 micron APS powder) to achieve 0, 1, 3, and 5- weight percentages. 2 g of Al_2O_3 and the respective amounts of metal precursor salt were dissolved in 10 mL of deionized water and labeled Bulk Al_2O_3, WAl_1%, WAl_3%, and WAl_5%, respectively; the solutions were continuously magnet stirred for 24 hours at room temperature, vacuum dried at room temperature for 24 h, and later calcined at 650 °C, over a ramp of 5 °C min^{-1} during 6 h. Lastly, the powder products were stored in a vacuum chamber.

2.2. Characterization

Thermogravimetric studies were performed to determine the possible phase transitions the ATT precursor salt could undergo during the calcination step of the NPs synthesis process. The weight and heat- flow changes were tracked through TGA- DSC performed on a TA Instruments SDT- Q600 thermobalance under an air flow of 100 mL min^{-1} within the 30 – 800 °C temperature range. The crystallographic studies of the nanomaterials were based on the XRD patterns obtained through a Philips X'Pert diffractometer in the Bragg- Brentano configuration using Cu K_α radiation (λ = 1.5406 Å) operated at 45 kV and 30 mA with a 0.02° min^{-1} step; data was collected from 20 to 80° 2θ. Crystallite size was calculated by fitting the peaks of the XRD patterns using the pseudo- Voigt function (PVF) in X'Pert Highscore Plus software and using the Scherrer formula. Crystallography of the materials was further examined by measuring the *d*- spacings of the diffraction rings and spots gathered through a JEOL JEM- 200 microscope in SAED mode.

Nanoparticle size distribution of the materials was determined from the TEM images obtained by the same microscope operated at an accelerating voltage of 200 kV. Morphology and size distribution of the agglomerates were determined over the SEM micrographs taken by a JEOL

JSM- 5300 microscope. The elemental composition of each sample, analyzed to rule out possible contamination during the synthesis of the materials, was performed by an Oxford Instruments EDS spectrometer coupled to the SEM. Textural properties (specific surface area, pore diameter, and pore volume) of the materials were evaluated by the nitrogen adsorption- desorption method using a Micrometrics Tristar 3000 analyzer at −196 °C and relative pressures (P/P_0) in the range of 0.0 – 1.0. Brunauer- Emmett- Teller specific surface areas (S_{BET}) were calculated from the N_2 adsorption data, and Barrett–Joyner–Halenda (BJH) pore volumes and pore size distribution were estimated from the N_2 desorption path of the isotherms of the freshly calcined catalysts. Before measurements, the samples were pretreated by degassing under vacuum at 120 °C for 30 min followed by another 3 h at 300 °C.

The oxidation states and composition of the sample surface were determined by XPS utilizing a SPECS Phoibos (DLD, HSA3500) spectrometer operating with an X- ray source from an aluminum anode at $K\alpha$ = 1486.6 eV; pass energy of 150 eV; working force of 4.48 eV, and an energy step of 1.0 eV. The carbon, C 1s, binding energy (BE) peak was calibrated at 284.5 eV as a charge- induced shifting correction.

The surface chemical reactivity of the materials was evaluated through the methanol (CH_3OH) dehydration to dimethyl ether (CH_3OCH_3, DME) reaction (Eq. 1) in a dynamic flow reactor at 275 °C and atmospheric pressure. 0.2 g of the catalyst were pretreated at 300 °C for 1 h in nitrogen flow (20 mL min^{-1}) to remove physisorbed water molecules. Methanol feed into the reactor was 0.33 mL h^{-1} with nitrogen as carrier gas (20 mL min^{-1}), achieving a weight hourly space velocity (WHSV) of 6099 mL g_{cat}^{-1} h^{-1}. The reaction products were analyzed by an HP 6890 Series I gas chromatograph equipped with a thermal conductivity detector and Supelcowax- 10 Bonded polyethylene glycol fused silica capillary column (30 m length, 0.53 mm I.D., and 0.5 mm film thickness). Methanol conversion (Con), DME selectivity (Sel), and DME yield were calculated with Equations 2 – 4. Byproduct generation was not observed and discarded after a mass balance assessment.

$$2CH_3OH \Leftrightarrow CH_3OCH_3 + H_2O, \qquad \Delta H_R^o = -24.1\ kJ\ mol^{-1} \tag{1}$$

$$Con_{CH_3OH}\ (\%) = \frac{[CH_3OH]_0 - [CH_3OH]_i}{[CH_3OH]_0} \times 100 \tag{2}$$

$$Sel_{DME}\ (\%) = \frac{[DME]}{[DME] + [Byproducts]} \times 100 \tag{3}$$

$$Yield = Con_{CH_3OH} \times Sel_{DME} \tag{4}$$

The surface acidity of the NPs was probed through TPD- NH_3 on a ChemBET Pulsar TPR/TPD piece of equipment. 100 mg of sample were pretreated by removing physisorbed water and organic molecules over a heating rate of 10 °C min^{-1} up to 550 °C under a 120 mL min^{-1} helium flow; next, they were cooled down to 50 °C at the same flow for 10 min. Excess NH_3 was removed at 50 °C in a helium atmosphere during 40 min. Finally, TPD profiles were recorded within the range of 100 to 800 °C with helium as gas carrier.

3. Results and discussion

3.1. Thermogravimetric analysis

The thermal decomposition of the precursor salt ATT depicts a path along four steps, as shown on the thermogram curves in Fig. 1. In the first step, 30 – 150 °C, a TGA weight reduction of 2 % was observed, attributed to the well- known physisorbed water, accompanied by an endothermic peak observed on the DSC thermogram. The second step occurred within the 190 – 285 °C temperature range as an endothermic process with a weight loss of 16 %. According to literature, this signal corresponds to the release of H_2S and NH_3 from ATT and the formation of some amorphous WS_2 [31 – 33]. The intense peak within 345 – 500 °C is inferred to involve the

WS_2 transformation to crystalline tungsten oxide, WO_3, represented by a total weight loss of 17 % including the assumed evolution of sulfur into SO and SO_2 which contributed to the last exothermic process, reaching a residual weight percentage of 65 % (67 % theoretical). According to these preliminary results, we could expect a crystalline tungsten oxide phase after the synthesis of the nanomaterials if metal load were high enough.

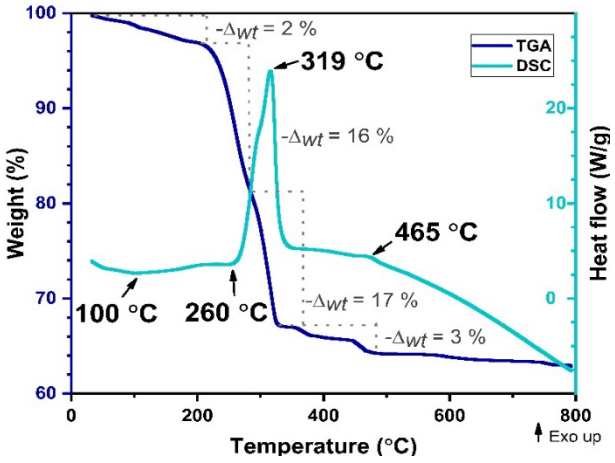

Fig. 1. Air TGA - DSC thermogram of ammonium tetrathiotungstate salt, ATT.

3.2. Crystallographic studies

The X- ray diffractograms acquired of the materials are shown in Fig. 2. The alumina support was found to be a mixture of gamma and delta phases, γ–δ–Al_2O_3. The 2θ peaks at 37, 39.5, 45.9, and 67.0 of all samples were matched to the cubic γ–Al_2O_3 phase (ICDD: 10- 0425), and the peak at 42.8 (marked by *) was matched to the tetragonal δ–Al_2O_3 phase (ICDD: 47- 1770); whereas no peaks could be ascribed to the tungsten component. The above proved high dispersion of the tungsten phase and no crystalline WO_3 present [34]. The diffraction peaks were indexed as the (311), (222), (400), and (440) crystal planes of γ–Al_2O_3 and as the (316) crystal plane of δ–Al_2O_3, respectively. The predominant peaks were used to calculate crystallite average size; the resulting sizes followed an increasing trend, 7.6 < 9.1 < 9.9 < 10.0 nm, as the tungsten weight percentage was raised.

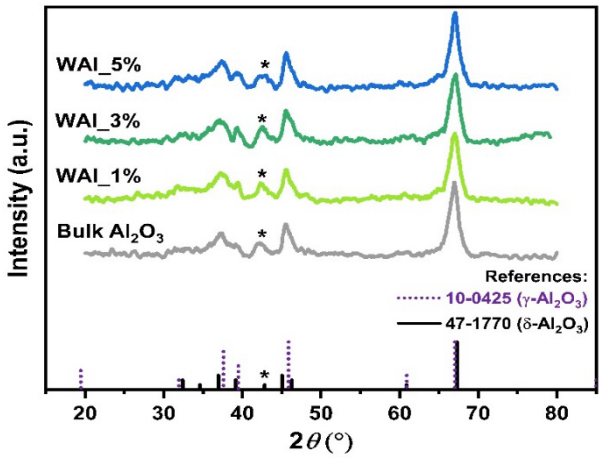

Fig. 2 X- ray diffractograms of the nanomaterials.

The SAED patterns of the samples corroborated the crystallographic XRD results. Representative SAED diffractograms are shown in Fig. 3. The measurements obtained from the diffraction rings and bright dots, 2.4 Å and 2.3 Å, are associated with the interplanar distances ascribed to the (311) and (222) planes, indexed at 37.6 and 39.5° 2θ of γ–Al_2O_3; the d- spacing of 1.4 Å was ascribed to overlapping diffraction angles at 67.0° of γ–Al_2O_3 and 67.3° of δ–Al_2O_3 as the (440) and (442) planes, respectively. The same interplanar distances were seen in all samples and no electron diffraction could be attributed to crystalline WO_3.

3.3. Morphology analyses

The TEM analysis disclosed the morphology of the nanoparticles as seen on the micrographs presented in Fig. 3. A quasispherical shape with crescent average size defined all nanoparticle samples as follows: 10.39 < 13.17 < 14.51 < 14.87 nm for Bulk Al_2O_3, WAl_1%, WAl_3%, and WAl_5%, respectively, whose size distribution is presented in the same figure. This growing tendency is aligned with the increasing tungsten weight percentage of the samples.

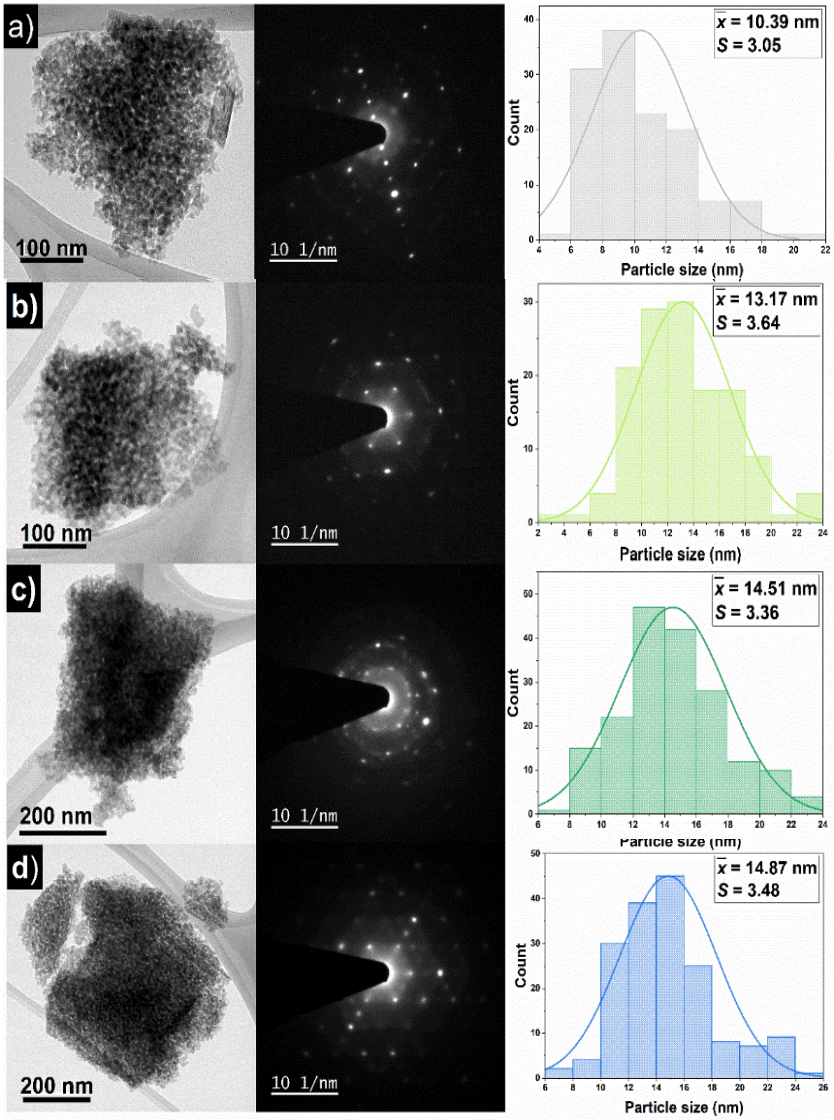

Fig. 3. Bright - field TEM micrographs, SAED patterns, and particle size distribution of a) Bulk Al_2O_3, b) WAl_1%, c), WAl_3%, and d) WAl_5% samples.

As can be seen in Fig. 4, the materials formed small, cracked clusters over flake- like aggregates. The morphology of the support did not undergo visible changes as the tungsten weight percentage was raised during synthesis. The elemental analyses performed through EDS depicted an almost directly proportional increase in W weight % as the concentration of its precursor compound was increased in each synthesis; the results are included in Table 1.

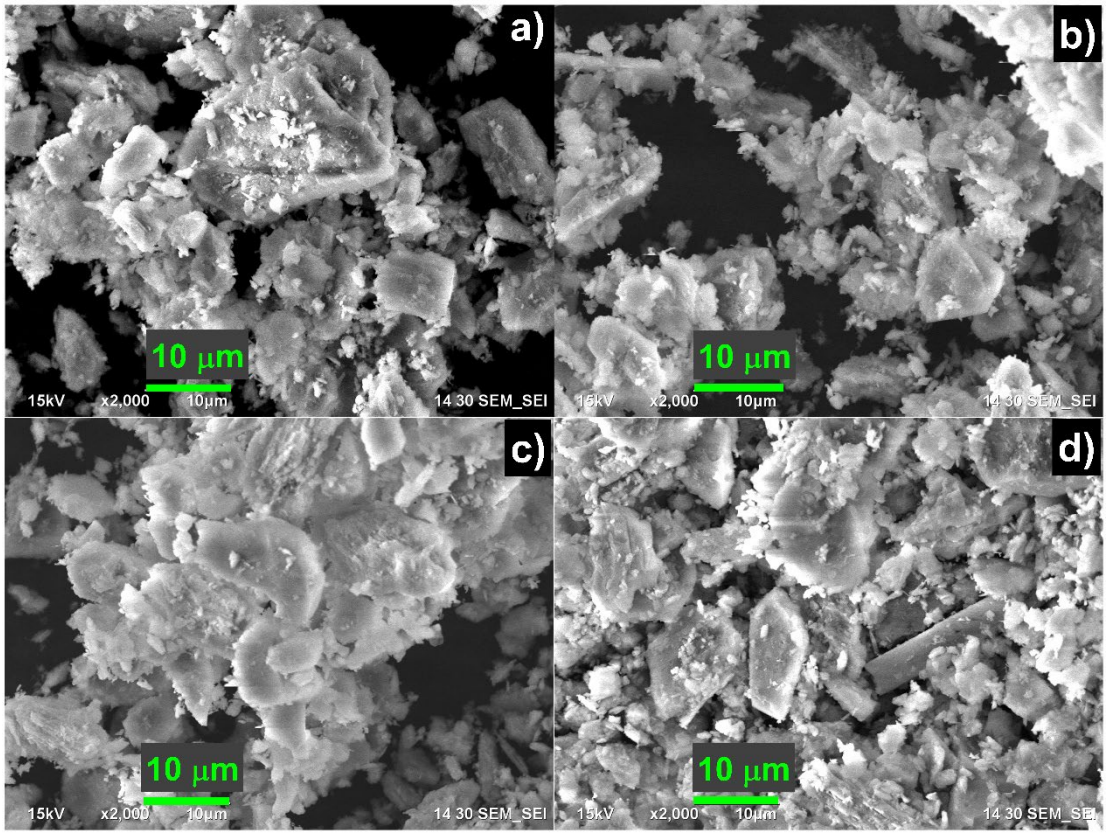

Fig. 4. SEM micrographs at 2000X of the nanomaterials.

3.4. Surface analyses

The textural surface properties of the nanomaterials are disclosed in Table 1. The surface area per gram of pure calcined alumina was 95.8 $m^2\ g^{-1}$, whereas for the material with 1 *wt* % metal load it resulted to be greater (97.4 $m^2\ g^{-1}$) since the material became slightly more porous with a 1.7 % decrease in pore diameter and a 1.0 % increase in total pore volume (both calculated through the BJH model of the desorption branch of the isotherm). Subsequently, as the metal oxide content was raised from 1 % to 5 %, the specific area decreased, 97.4 > 95.5 > 91.2 $m^2\ g^{-1}$, alongside pore volume and size, possibly due to the occlusion of these components into the alumina structure affecting its textural properties [35]. The N_2 adsorption- desorption behavior of the nanomaterials was identified as Type IV- H1 according to the IUPAC classification of adsorbents with delayed capillary condensation and evaporation on mesopores (2 – 50 nm pore diameter) of cylindrical or ordered three- dimensional shape as depicted through the hysteresis loop displayed by all materials and proven by the average pore diameter, 6.7 nm [36].

The tungsten metal surface density (ρ_W), W atoms per specific surface area [W nm^{-2}], of the nanoparticles was calculated as function of metal oxide (WO_3) weight percent and specific surface area [16]. The materials proved to have below monolayer coverage, <5 W nm^{-2}; results are included in Table 1.

Table 1. Composition[a], textural properties[b], and tungsten metal surface density[c] of the nanomaterials.

Sample	*wt* %		S_{BET}	V_p	D_p	ρ_W
	Nominal	Measured	($m^2\ g^{-1}$)	($cm^3\ g^{-1}$)	(nm)	(W nm^{-2})
Bulk γ–δ–Al_2O_3	—	—	95.8	0.200	6.8	—
WAl_1%	1	1.2	97.4	0.202	6.7	0.3
WAl_3%	3	2.5	95.5	0.195	6.6	0.7
WAl_5%	5	4.1	91.2	0.188	6.5	1.2

[a]Nominal weight percentage and weight percentage measured by EDS
[b]Specific surface area (S_{BET}), cumulative pore volume (V_p), and average pore diameter (D_p)
[c]Metal tungsten oxide surface density (ρ_W)

For the chemical surface characterization of the nanomaterials, XPS analyses were conducted; the representative spectra of sample WAl_5% are illustrated in Fig 5.

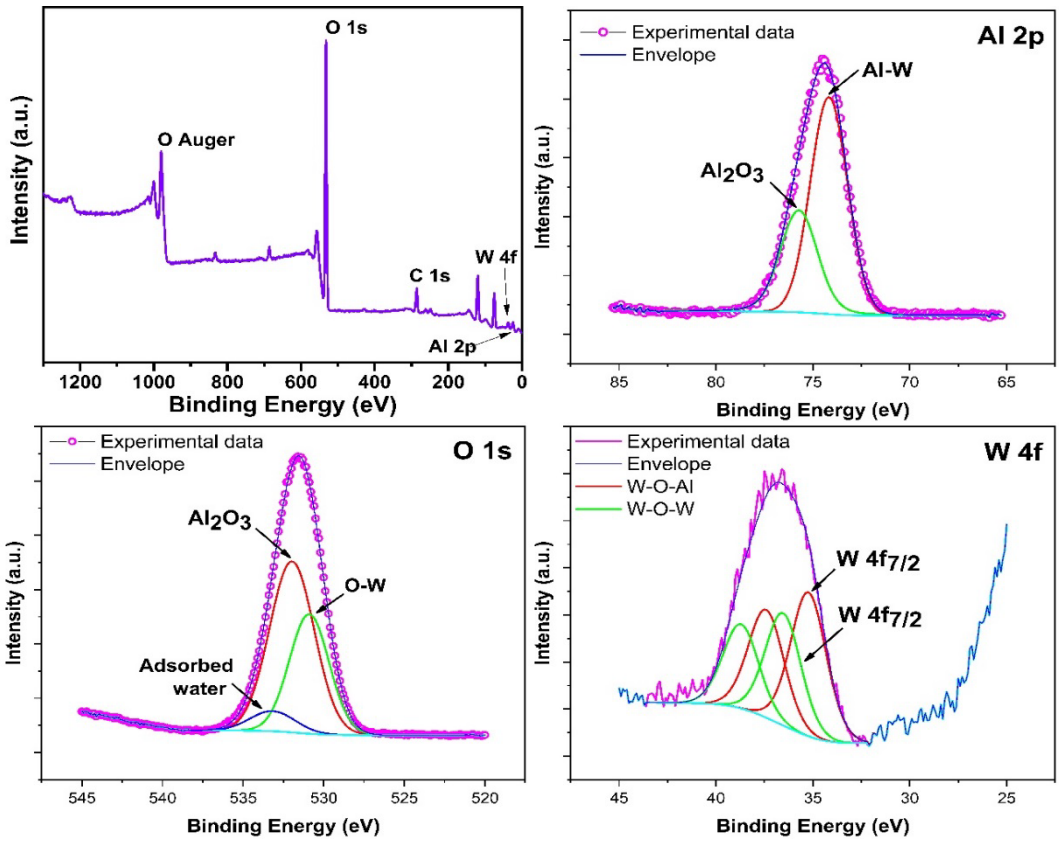

Fig. 5. XPS survey and high - resolution spectra of the representative, fresh WAl_5% sample.

The XPS survey of all samples showed the presence of only the expected elements, O, Al, and W. The high- resolution spectra of Al (Al 2p), O (O 1s), and W (W 4f) were processed considering a Shirley background. Al 2p was deconvoluted into two peaks (with a goodness- of- fit figure of merit, residual STD, equal to 1.1 ± 0.1) located at binding energies (BE) of 74.1 and 75.5 eV associated with the Al–W and Al_2O_3 components, respectively [14, 37 – 38]. O 1s was deconvoluted into 3 peaks (RSTD = 1.5 ± 0.2) at 530.9, 532.0, and 533.2 eV, corresponding to W–O, Al_2O_3, and adsorbed water, respectively [14; 39]. The tungsten spectrum was deconvoluted into two pairs of the W $4f_{5/2}$ and W $4f_{7/2}$ well- separated, spin- orbit doublets (Δ_{BE} = 2.18 eV) with a

symmetrical Gaussian (70 %) – Lorentzian (30 %) product formula, GL(30), and an area ratio constraint of 3:4 (RSTD = 0.98 ± 0.02). The FWHM values of the peaks were found to be within the range of 2.18 to 2.20 eV due to the metal- oxide nature of the sample and in agreement with literature [39]. The binding energy for W $4f_{7/2}$ at 36.5 eV was assigned to the W–O–W species (Species 1); whereas, the BE assigned to Species 2, W–O–Al, was downshifted to 35.2 eV due to the chemical environment involving different W–Al bond length, bond angle, and electronegativity [11, 14, 40].

To further investigate the surface of the materials through their chemical properties, the area under each doublet pair curves for Species 1 and Species 2 was determined and expressed in percentages (Table 2.) to evaluate the correlation between surface tungsten species and reactivity performance in the dehydrogenation reaction of methanol to dimethyl ether.

The chemical evaluation for this reaction was carried out at 275 °C in a fixed- bed, steady- state reactor to probe the conversion of methanol (*Con* %); the selectivity to DME was found to be 100 % for all materials; the results are included in Table 2. Bulk Al_2O_3 reached a 23 % conversion; and as metal load was raised, the nanomaterials conveyed an increasing conversion up to 45 %, which could be correlated to an increment of the Species 2 percentage.

Table 2. Chemical properties of the materials.

Sample	*Con %*[a]	XPS Intensity[b] %		Acid Sites[c]			
		Species 1	Species 2	Weak %	Medium %	Strong %	Total ($\mu mol_{NH3}\ g_{cat}^{-1}$)
Bulk γ–δ–Al_2O_3	23	0	0	0	50	50	54
WAl_1%	35	45	55	0	32	68	37
WAl_3%	44	44	56	7	58	35	32
WAl_5%	45	40	60	5	67	28	29

[a]Methanol conversion to DME
[b]Percentage of area under each spin- orbit doublet pairs
[c]Acidity evaluated by TPD- NH_3

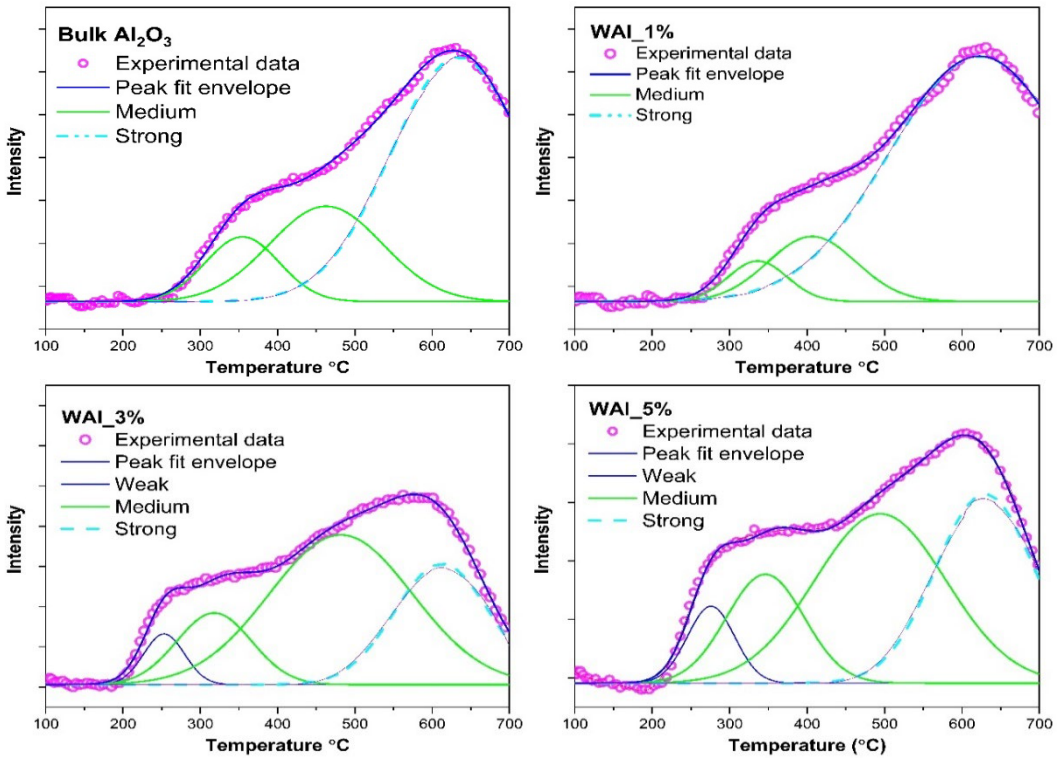

Fig. 6. TPD- NH_3 profiles for all nanomaterials.

The acidity of the nanomaterials was also defined by ammonia desorption as function of temperature to additionally describe the nature of the surface active sites; the results are included in Table 2 and the TPD- NH_3 profiles can be observed in Figure 6. Total Lewis and Brønsted acidity per gram of material was disclosed to be higher for bulk Al_2O_3 in comparison to the metal loaded alumina samples. Nevertheless, after defining the acidic nature in terms of strength as weak (150 – 300 °C), medium (300 – 500 °C), and strong (> 500 °C) [41], and allocating the respective percentages, it was interesting to observe that bulk Al_2O_3 and the material closest to it with the lowest metal load (WAl_1%) had only medium and strong acidic sites, whereas samples WAl_3% and WA_5% also manifested weak acidic character, to which the higher methanol conversion could be attributed as it is known that methanol dehydration to DME preferably occurs on weak acidic Brønsted sites [26, 27, 30, 42].

4. Conclusions

In conclusion, the nanomaterials herein synthesized of supported tungsten oxides were characterized and found to have no crystalline tungsten surface components. XRD and SAED studies elucidated the mixed crystalline phase of alumina, γ–δ–Al_2O_3, as was expected since metal load was kept below monolayer (< 5 W nm^{-2}) by using low metal weight percentages for the preparation of the materials. On the basis of the well- known coordination geometry of tungsten oxide as function of metal load coverage on the support, in this study the tetrahedral, octahedral, and distorted- octahedrally coordinated components were rather grouped by their electronic character as disclosed by XPS analyses into W–O–W and W–O–Al species, Species 1 and Species 2, respectively.

The amount percentage of Species 2 was correlated to the chemical performance of the materials in the methanol dehydration reaction to dimethyl ether; as the former increased, so did the latter. Moreover, the methanol conversion was correlated to the appearance of weak acidic sites after 3 and 5 % weight metal loading. Lastly, the interaction between the surface tungsten species and the support is more reaching than the interaction of the tungstate components among themselves as was made manifest by a better chemical reactivity and the weakening of the support so as to perform better in acidic relying reactions. This research sheds light on the intricate interaction between surface tungsten species and the support, enhancing the understanding of these nanomaterials and their potential applications, mainly in catalytic reactions.

Acknowledgments

We express our sincere gratitude to E. Aparicio, P. Casillas, I. Gradilla, Dr. D. Domíguez, Dr. R. Valdez, Dra. A. Garzón, and Dr. M. Ávalos for their invaluable technical support and input. We also acknowledge the financial backing granted through the DGAPA PAPIIT Grant No. IG100823.

References

[1] S. Yue, H. Pan, Z. Ning, J. Yin, Z. Wang, G. Zhang, Nanotechnology, **22** (11), 115703 (2011); https://doi.org/10.1088/0957-4484/22/11/115703
[2] L.G. Teoh, J. Shieh, W.H. Lai, I.M. Hung, M.H. Hon, Journal of Alloys and Compounds, **396** (1–2), 251 (2005); https://doi.org/10.1016/J.JALLCOM.2004.12.005
[3] M.B. Tahir, S. Ali, M. Rizwan, International Journal of Environmental Science and Technology, **16** (8), 4975 (2019); https://doi.org/10.1007/s13762-019-02385-5
[4] V. Dutta, S. Sharma, P. Raizada, V.K. Thakur, A.A.P. Khan, V. Saini, A.M. Asiri, P. Singh, Journal of Environmental Chemical Engineering, **9** (1), 105018 (2021); https://doi.org/10.1016/J.JECE.2020.105018
[5] J.C. Murillo-Sierra, A. Hernández-Ramírez, L. Hinojosa-Reyes, J.L. Guzmán-Mar, Chemical

Engineering Journal Advances, **5** 100070 (2021); https://doi.org/10.1016/j.ceja.2020.100070
[6] Hamed Bateni, Chad Able, Catalysis in Industry, **11** (1), 7 (2019); https://doi.org/10.1134/S2070050419010045
[7] N. Mota, E.M. Ordoñez, B. Pawelec, J.L.G. Fierro, R.M. Navarro, Catalysts, **11** (4), (2021); https://doi.org/10.3390/catal11040411
[8] T. Aihara, K. Asazuma, H. Miura, and T. Shishido, RSC Advances, **10** (61), 37538 (2020); http://dx.doi.org/10.1039/D0RA08340B
[9] W. Grünert, R. Feldhaus, K. Anders, E.S. Shpiro, K.M. Minachev, Journal of Catalysis, **456** 522 (1989)
[10] N. Liu, S. Ding, Y. Cui, N. Xue, L. Peng, X. Guo, and W. Ding, Chemical Engineering Research and Design, **91** (3), 573 (2013); http://dx.doi.org/10.1016/j.cherd.2012.08.008
[11] J.F. Wu, A. Ramanathan, A. Biancardi, A.M. Jystad, M. Caricato, Y. Hu, B. Subramaniam, ACS Catalysis, **8** (11), 10437 (2018); http://dx.doi.org/10.1021/ACSCATAL.8B03263
[12] A. Jain, A. Ramasubramaniam, Physical Chemistry Chemical Physics, **20** (36), 23262 (2018). http://dx.doi.org/10.1039/C8CP04113J
[13] M. Vasilopoulou, A. Soultati, D.G. Georgiadou, T. Stergiopoulos, L.C. Palilis, S. Kennou, N.A. Stathopoulos, D. Davazoglou, P. Argitis, Journal of Materials Chemistry A, **2** (6), 1738 (2014); http://dx.doi.org/10.1039/c3ta13975a
[14] X. Xu, S. Liu, Y. Cui, X. Wang, K. Smith, Y. Wang, Catalysts, **9** (4), (2019); http://dx.doi.org/10.3390/catal9040389
[15] F. Di-Grégorio, V. Keller, T. Di-Costanzo, J.L. Vignes, D. Michel, and G. Maire, **218** 13 (2001); https://doi.org/10.1016/S0926-860X(01)00587-7
[16] E.I. Ross-Medgaarden, W. V. Knowles, T. Kim, M.S. Wong, W. Zhou, C.J. Kiely, I.E. Wachs, Journal of Catalysis, **256** (1), 108 (2008); https://doi.org/10.1016/J.JCAT.2008.03.003
[17] A.I. Osman, J.K. Abu-Dahrieh, D.W. Rooney, S.A. Halawy, M.A. Mohamed, A. Abdelkader, Applied Catalysis B: Environmental, **127** 307 (2012); http://dx.doi.org/10.1016/j.apcatb.2012.08.033
[18] K.T. Ng, D.M. Hercules, Journal of Physical Chemistry, **80** (19), 2094 (1976); https://pubs.acs.org/doi/epdf/10.1021/j100560a009
[19] R. Thomas, F.P.J.M. Kerkhof, J.A. Moulijn, J. Medema, V.H.J. de Beer, Journal of Catalysis, **61** 559 (1980)
[20] L. Salvati, L.E. Makovsky, J.M. Stencel, F.R. Brownls, D.M. Hercules, Journal of Physical Chemistry, **85** 3700 (1981); https://doi.org/10.1021/j150624a035
[21] T. Kim, A. Burrows, C.J. Kiely, I.E. Wachs, Journal of Catalysis, **246** (2), 370 (2007); https://doi.org/10.1016/j.jcat.2006.12.018
[22] L.L. Murrell, D.C. Grenoble, R.T.K. Baker, E.B. Prestridge, S.C. Fung, R.R. Chianelli, S.P. Cramer, Journal of Catalysis, **79** (1), 203 (1983); https://doi.org/10.1016/0021-9517(83)90303-2
[23] J.A. Horsley, I.E. Wachs, J.M. Brown, G.H. Via, F.D. Hardcastle, Journal of Physical Chemistry, **91** (15), 4014 (1987); https://doi.org/10.1021/j100299a018
[24] D. Soung Kim, M. Ostromecki, I.E. Wachs, Journal of Molecular Catalysis A: Chemical, **106** 93 (1996); https://doi.org/10.1016/1381-1169(95)00186-7
[25] M.L. Luna, L. Cedeño-Caero, Journal of Applied Research and Technology, **16** (6), 455 (2018); https://doi.org/10.22201/icat.16656423.2018.16.6.744
[26] A. Guntida, K. Suriye, J. Panpranot, P. Praserthdam, Catalysis Today, **358** 354 (2020); https://doi.org/10.1016/j.cattod.2019.07.019
[27] M. Saito, T. Aihara, H. Miura, T. Shishido, Catalysis Today, **375** 64 (2020); https://doi.org/10.1016/j.cattod.2020.02.009
[28] I.E. Wachs, C.C. Chersich, J.H. Hardenbergh, Applied Catalysis, **13** 335 (1985); https://doi.org/10.1016/S0166-9834(00)81152-5
[29] G. Ramis, C. Cristiani, A.S. Elmi, P. Villa, G. Busca, Journal of Molecular Catalysis, **61** (3), 319 (1990); https://doi.org/10.1016/0304-5102(90)80006-5
[30] A. El-Aziz, A. Said, M.M.M. Abd El-Wahab, M. Abd El-Aal, Chemical and Materials Engineering, **4** (2), 17 (2016)
[31] R.J.H. Voorhoeve, H.B.M. Wolters, ZAAC-Journal of Inorganic and General Chemistry, **376** (2), 165 (1970); https://doi.org/10.1002/zaac.19703760210

[32] D. Hunyadi, A.L. Vieira Machado Ramos, I.M. Szilágyi, Journal of Thermal Analysis and Calorimetry, **120** (1), 209 (2015); https://doi.org/10.1007/s10973-015-4513-4
[33] J. Espino, L. Alvarez, C. Ornelas, J.L. Rico, G. Berhault, Catalysis Letters, **90** (1–2), 71 (2003); https://doi.org/10.1023/A:1025820427669
[34] M. Smyrnioti, T. Ioannides, Catalysts, **12** (4), (2022); https://doi.org/10.3390/catal12060604
[35] K. V. Manukyan, A. V. Yeghishyan, C.E. Shuck, D.O. Moskovskikh, S. Rouvimov, E.E. Wolf, A.S. Mukasyan, Microporous and Mesoporous Materials, **257** 175 (2018). https://doi.org/10.1016/j.micromeso.2017.08.044
[36] M. Thommes, K. Kaneko, A. V Neimark, J.P. Olivier, F. Rodríguez-Reinoso, J. Rouquerol, K.S.W. Sing, Pure and Applied Chemistry, **87** (9–10), 1051 (2015); h https://doi.org/10.1515/pac-2014-1117.
[37] J.A. Rotole, P.M.A. Sherwood, Surface Science Spectra, **5** (1), 18 (1998); https://doi.org/10.1116/1.1247852
[38] J. Van den Brand, P.C. Snijders, W.G. Sloof, H. Terryn, J.H.W. De Wit, Journal of Physical Chemistry B, **108** (19), 6017 (2004); https://doi.org/10.1021/jp037877f
[39] B. Vincent Crist, Handbooks of Monochromatic XPS Spectra, Volume 2 – Commercially Pure Binary Oxides and a few Common Carbonates and Hydroxides, XPS International, LLC, (2005); www.xpsdata.com
[40] A. Mozalev, M. Bendova, F. Gispert-Guirado, Z. Pytlicek, E. Llobet, Journal of Materials Chemistry A, **4** (21), 8219 (2016); https://doi.org/10.1039/C6TA02027E
[41] S. Mosallanejad, B.Z. Dlugogorski, E.M. Kennedy, M. Stockenhuber, ACS Omega, **3** (5), 5362 (2018); https://doi.org/10.1021/acsomega.8b00201
[42] T. Kitano, T. Hayashi, T. Uesaka, T. Shishido, K. Teramura, T. Tanaka, ChemCatChem, **6** (7), 2011 (2014); https://doi.org/10.1002/cctc.201400053